Supporting Information

Noble-metal-free π-stacked metal–organic nanosheets featuring unidirectional electron transport channels for highly efficient electrocatalytic CO_2 reduction

Qiuping Xie, Yunxiang He, Qinling Liu, Siqi Deng, Xiaoling Wang, Wen Liao, Gonghua Hong*, Ian Manners† & Junling Guo*

*Corresponding authors

†Deceased December 3rd, 2023

Table of Contents

Section S1. Materials and methods

Materials

Ellagic acid ($C_{14}H_6O_8$, 97% purity) was acquired from Acros Organics (Belgium). Bismuth nitrate pentahydrate ($Bi(NO_3)_3 \cdot 5H_2O$, 99%) and *N*-methyl-2-pyrrolidone (NMP, 99%) were supplied by Chron Chemicals (China). Absolute ethanol was procured from General Reagents. All chemicals were utilized without further purification. Ultrapure water (18.2 MΩ·cm resistivity) was generated using a Merck Millipore Elix water purification system. Freshly prepared aqueous solutions were employed in all experimental procedures.

Preparation of Bi-EA mesocrystals

Ellagic acid (EA, 0.26 mmol) and bismuth nitrate pentahydrate ($Bi(NO_3)_3 \cdot 5H_2O$, 0.52 mmol) were dissolved in 25 mL of *N*-methyl-2-pyrrolidone (NMP) at room temperature under ambient atmosphere without stirring. The resulting solution was then allowed to age under static conditions for 7 days, during which a light-yellow precipitate gradually formed.

The precipitate was collected by centrifugation at 2000 rcf for 5 min, washed once with NMP (50 mL) and twice with ethanol (2 × 50 mL) to remove residual solvent and unreacted species, and recollected by centrifugation at 2000 rcf for 5 min after each washing step. The final product was dried under vacuum at 40 ℃ to obtain the Bi-EA mesocrystals.

Preparation of MPhene

The *MPhene* nanosheets were synthesized through liquid-phase exfoliation of bulk Bi-EA mesocrystals using ultrasonic processing. During solvent-assisted delamination, polar molecules penetrate interlayer galleries, weakening van der Waals forces to yield two-dimensional nanostructures. For the standard procedure, 10 mg of precursor crystals were dispersed in 1 mL of ethanol within a 20 mL glass vessel. Ultrasonication was performed at 50 W output (40 kHz frequency) in a temperature-controlled bath (298 K) for 30 min. Subsequent centrifugation at 4000 rcf (10 min, 298 K) removed unexfoliated aggregates.

Powder specimens were prepared by concentrating 50 mL colloidal suspensions via rotary evaporation (40 ℃, reduced pressure), followed by lyophilization to obtain dry *MPhene* samples for spectroscopic characterization (FT-IR, XPS, Raman).

Deposition of MPhene on mica substrates

Mica substrates (5 mm × 5 mm) were pretreated by washing with deionized water and ethanol (high-performance liquid chromatography grade) repeatedly and drying under a flow of N_2. Then, the fresh mica substrates exfoliated by tape were used in the next process. A drop of dispersion (30 μL) containing the prepared *MPhene* was placed on the pretreated mica substrate and then allowed to dry naturally in air before characterization.

Section S2. General characterizations

Instruments and software

Crystalline structures of *MPhene* nanosheets were analyzed via powder X-ray diffraction (Rigaku Miniflex 600, Japan) employing Cu Kα radiation (λ = 0.15418 nm). Raman spectroscopic measurements were conducted using a HORIBA HR800 spectrometer (France) with 532 nm laser excitation, scanning from 200 to 2000 cm^{-1}. Morphological examination

was performed through field-emission scanning electron microscopy (Hitachi S-4800, Japan) and transmission electron microscopy (JEOL 2100F, 200 kV). Surface chemical states were determined by X-ray photoelectron spectroscopy (Thermo Scientific ESCALAB 250Xi) with Mg Kα radiation (1253.6 eV) at 31.5 eV pass energy. Atomic force microscopy images were captured using a Bruker Dimension Icon system. Mass spectrometric analysis was executed on a Bruker solariX 70 FT-MS instrument in positive and negative ion modes, with samples (1 μL, 0.5 mg mL^{-1}) introduced via electrospray ionization using 1:1 (v/v) water/acetonitrile mobile phase. Nuclear magnetic resonance spectra were acquired on a Bruker Ascend TM 600 MHz spectrometer. Optical properties were evaluated by UV-Vis spectroscopy (PerkinElmer LAMBDA 1050).

Electrochemical measurements

The CO_2RR performance of various samples was evaluated using a three-electrode flow cell system in a CO_2-saturated 0.5 M $KHCO_3$ aqueous solution. All electrochemical measurements were conducted on a CHI 760E electrochemical workstation (CH Instrument, Shanghai, China). The CO_2RR performance was measured after achieving stable linear sweep voltammetry (LSV) scanning. The working electrode (WE) consisted of approximately 0.3 mg of catalyst deposited on a gas diffusion layer with a 1 cm^2 working area. The reference electrode (RE) employed was an Ag/AgCl electrode, and the counter electrode (CE) utilized a platinum plate. During the electrochemical measurements, CO_2 was continuously pumped into the cathode chamber at a constant flow rate of 20 mL min^{-1}. The gas products were detected in situ using a connected gas chromatograph instrument (PANNA, A91 Plus). The liquid products were analyzed using a nuclear magnetic resonance (NMR) spectrometer (Bruker Ascend TM 600 MHz). The Faradaic efficiency (FE) during the CO_2RR was calculated using the equation $FE = Q_i/Q_t = (N_i \times n \times F)/Q_t$, where Q_i is the charge amount for product reduction, Q_t is the total charge consumed, N_i is the molar amount of the product, n is the number of electrons transferred (2 for formic acid, H_2, and CO), and F is the Faradaic constant (96,485 C mol^{-1}).

The normalized current density for HCOOH generation, denoted as $j_{normalized\ HCOOH}$, was calculated using the equation: $j_{normalized\ HCOOH} = j_{HCOOH}/A$, where A ($cm^2$) represents the electrochemical surface area (ECSA) of the catalyst per unit geometric electrode area (1 cm^2).

The ECSA of the catalysts was estimated from the electrochemical double-layer capacitance (C_{dl}) obtained by cyclic voltammetry (CV) measurements (Fig. S18†). CV curves were recorded in a non-Faradaic potential region at various scan rates (20–100 mV s^{-1}). The ECSA was then calculated using the following equation:

$$\mathrm{ECSA} = \frac{C_{dl}}{C_s}$$

where C_{dl} (mF cm^{-2}) is the double-layer capacitance, and C_s (0.04 mF cm^{-2}) is the specific capacitance of a smooth planar surface in aqueous electrolytes, based on literature reports.[1] Using this method, the C_{dl} values of *MPhene* nanosheets and Bi-EA mesocrystals were determined to be 5.91 and 0.81 mF cm^{-2}, corresponding to ECSA values of 147.75 and 20.25 cm^2, respectively.

The turnover frequency (TOF) for HCOOH production was quantified using the equation: $TOF = j_{HCOOH}/(F \times N \times n_e)$, where j_{HCOOH} (A cm^{-2}) is the partial current density for HCOOH

generation, n_e is the number of electrons transferred (2 for HCOOH), F is the Faradaic constant (96,485 C mol^{-1}), and N (mol cm^{-2}) denotes the active site density, which was determined as follows: a catalyst loading of 0.3 mg was deposited onto a 1 cm^2 working electrode, corresponding to a mass loading of 3×10^{-4} g cm^{-2}, and the relative atomic mass of bismuth is 208.98 g mol^{-1}. Based on prior research reporting a bismuth (Bi) mass content of 46.3% (verified via inductively coupled plasma optical emission spectroscopy, ICP-OES),[2] the areal density of Bi atoms was calculated as: $N = 6.647 \times 10^{-7}$ mol cm^{-2}. In this calculation, all Bi atoms were treated as potentially active sites; therefore, the resulting TOF values are apparent values.

In situ Raman measurements

In situ Raman measurements were performed using a custom-designed electrochemical cell that was connected to an electrochemical workstation. The three-electrode system (WE, RE, and CE) and the electrolyte used were the same as those employed in the previous electrochemical measurements. Before the Raman measurements, CO_2 was bubbled into the electrolyte. In situ Raman spectra were obtained using a confocal Raman spectroscopy setup (Alpha300, WITec) with a 532 nm laser as the excitation source.

XAFS measurements

The X-ray absorption fine structure (XAFS) experiments were conducted at beamline BL14W1 of the Shanghai Synchrotron Radiation Facility (SSRF), where the electron storage ring maintained an operating energy of 3.5 GeV. Radiation monochromatization was achieved through a silicon (311) double-crystal configuration. A solid-state fluorescence detector recorded spectral data at room temperature without environmental controls. Beam dimensions were precisely defined to 1 × 4 mm^2 through adjustable horizontal and vertical slit systems. Energy calibration referenced the absorption edge of bismuth metal powder standards. Fluorescence yield detection mode was employed for all measurements, with each scan repeated 2–3 times to ensure data reproducibility.

DFT calculations

The structural and electronic characteristics of *MPhene* were comprehensively examined through first-principles calculations performed in the ABACUS software environment, employing an all-electron density functional theory approach with numerical atomic orbital basis sets. Initial geometry optimization involved constructing a triclinic *P*1 unit cell from molecular mechanics-derived building blocks, with lattice parameters subsequently refined against high-resolution synchrotron X-ray diffraction patterns (λ = 0.6199 Å) using Rietveld analysis incorporating asymmetric Pseudo-Voigt peak profiles modified by Berrar-Baldinozzi corrections. Electronic structure computations utilized the Perdew-Burke-Ernzerhof generalized gradient approximation with optimized norm-conserving Vanderbilt pseudopotentials, implementing double-zeta polarized basis functions (NAO-VPS-2z2p) at 150 Ry kinetic energy cutoff, while Brillouin zone integration employed Monkhorst-Pack grids (3 × 3 × 1 for structural relaxation at 0.02 eV $Å^{-1}$ force tolerance; 4 × 4 × 1 for property calculations with 10^{-5} eV self-consistent field convergence). Electrochemical stability was assessed through the computational hydrogen electrode formalism, including implicit

solvation effects, followed by post-processing analysis of electronic density distributions via Bader partitioning and density of states decomposition using Slater-type orbital transformations.

Conductive atomic force microscopy (CAFM) measurements

CAFM analyses were conducted on a Cypher S instrument (Oxford Instruments/Asylum Research). A uniform layer of *MPhene* was obtained by dispensing its dispersion onto freshly cleaved highly oriented pyrolytic graphite (HOPG) through controlled pipetting. After drying, the specimen was fixed onto the AFM platform for characterization. Measurements employed contact-mode operation with a platinum-coated silicon cantilever (Olympus OMCL-AC240TM; nominal resonance frequency ~180 kHz; spring constant 40 N m^{-1}). During scanning, a 500 mV direct-current potential was applied to the substrate. The imaging parameters were adjusted to a 0.5 Hz line rate across a 5 μm × 5 μm field while maintaining the applied load below 20 nN to avoid tip-induced alterations. Simultaneous current detection was achieved using the ORCA™ module, and electrostatic isolation was implemented to suppress ambient electrical noise.

Section S3. Supporting figures

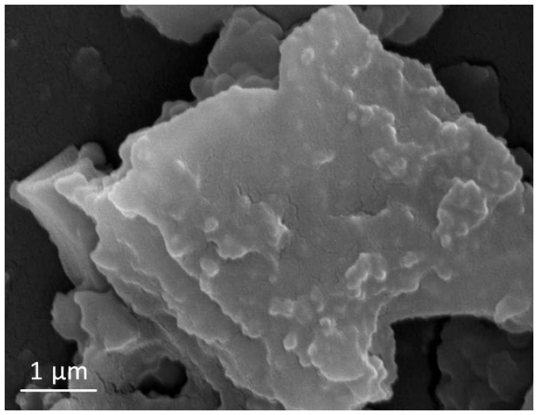

Fig. S1. SEM image of Bi-EA mesocrystals showing stacked, plate-like external morphologies.

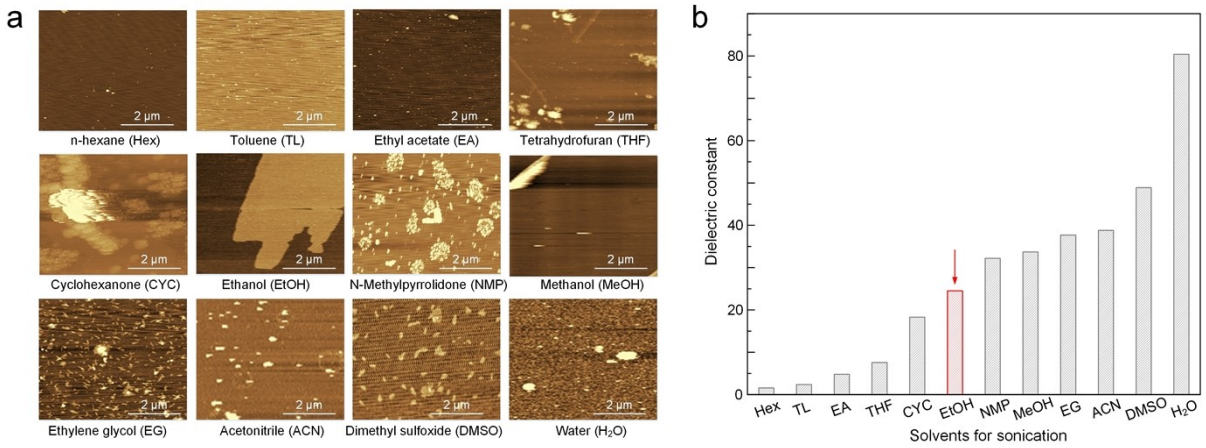

Fig. S2. (a) AFM images of Bi-EA mesocrystals after sonication-assisted exfoliation in different solvents. (b) Dielectric constants of the corresponding solvents used for exfoliation. Exfoliation was conducted under identical conditions (40 kHz, 50 W, 30 min, 298 K).

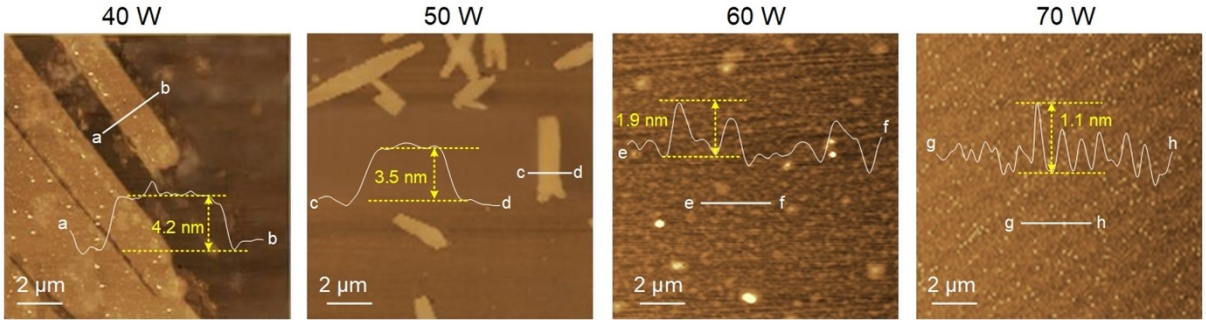

Fig. S3. AFM images of *MPhene* nanosheets obtained under different sonication powers.

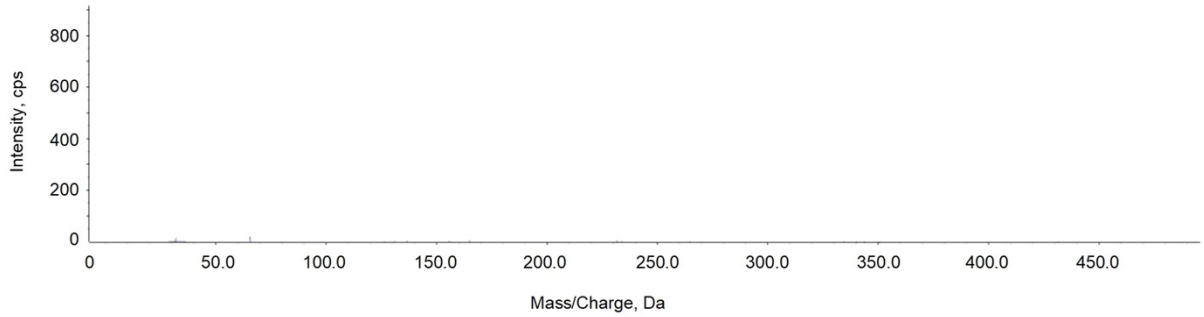

Fig. S4. Electrospray ionization mass spectrometry (ESI-MS) of ethanol suspensions of *MPhene* after 30 days. The lack of signals suggested that discrete molecules or metal ions were not present in the solution, confirming the structural stability of *MPhene*.

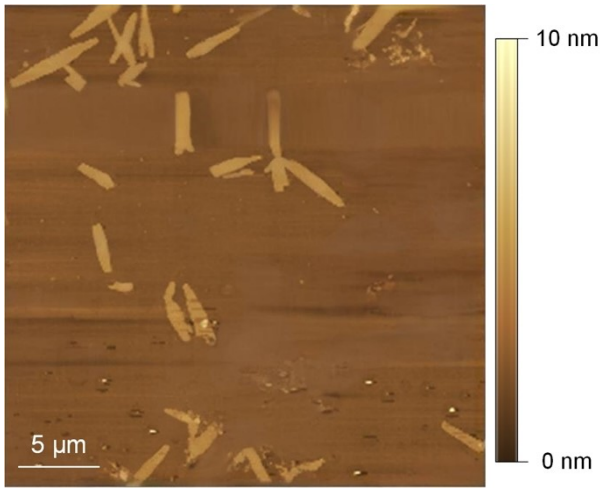

Fig. S5. AFM image of *MPhene* nanosheets under larger scan areas.

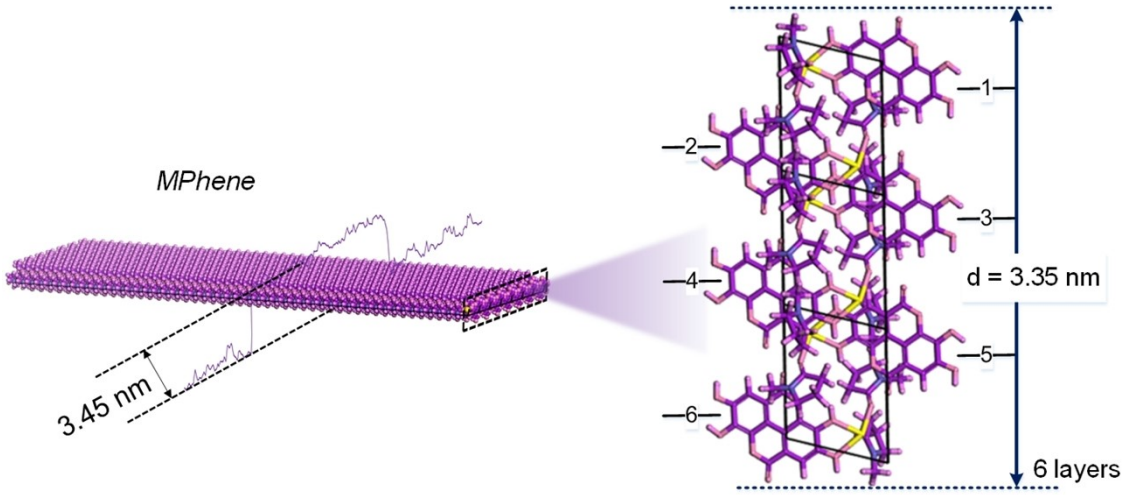

Fig. S6. Structure analysis of *MPhene* along the out-of-plane direction. Theoretical calculations showed that the *MPhene* consisted of 6 molecular layers (3.35 nm), which was nearly the same as the measured thickness from AFM experiments (3.45 nm).

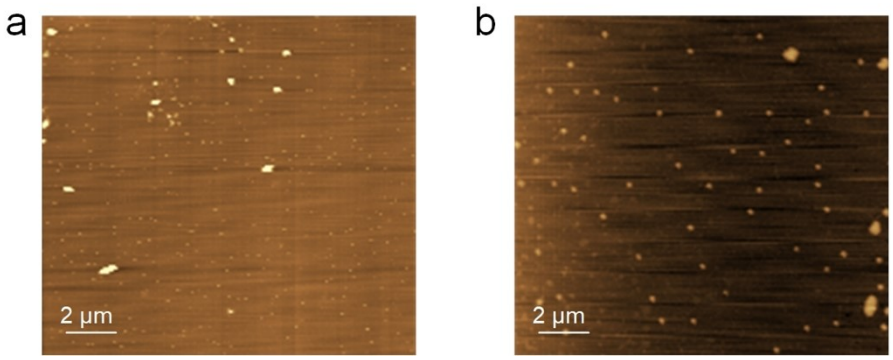

Fig. S7. AFM images of Bi-EA mesocrystals after (a) prolonged sonication (40 min) and (b) sonication at higher power (60 W). Irregular particles were observed under both conditions.

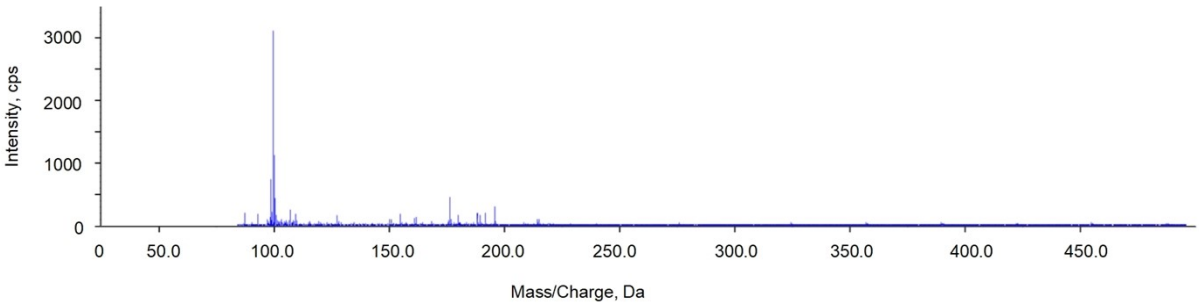

Fig. S8. Mass spectrum of acid-dissociated *MPhene* by ESI-MS. The fragment peak of about 100.1 indicated the presence of NMP molecules in the nanosheets.

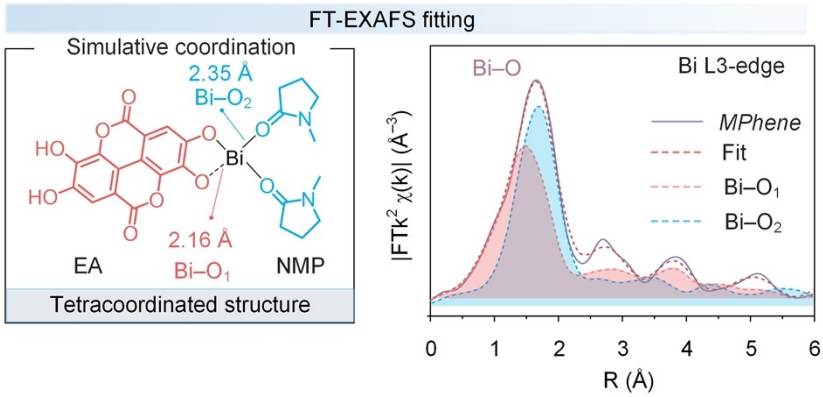

Fig. S9. Bi L3-edge k^2-weighted FT-EXAFS spectra and corresponding fitting in R-space (right), along with the proposed coordination structure (left) of *MPhene* nanosheets.

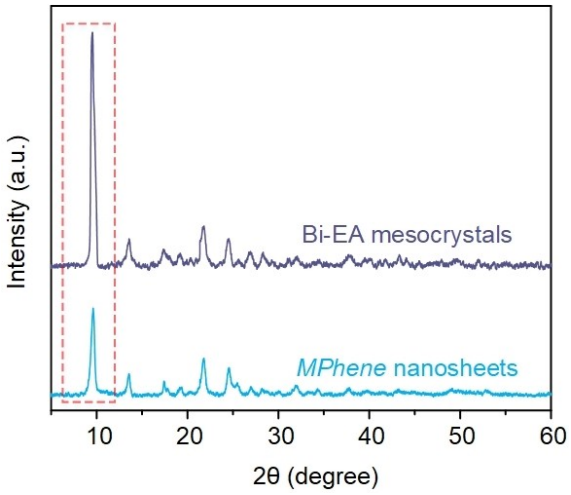

Fig. S10. PXRD patterns of bulk Bi-EA mesocrystals and exfoliated *MPhene* nanosheets.

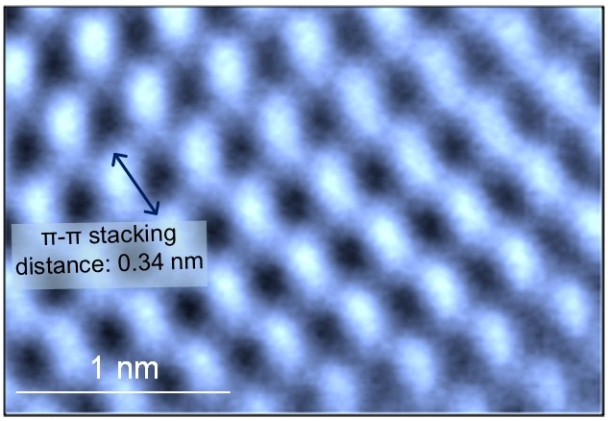

Fig. S11. HRTEM image of *MPhene* nanosheets with structural annotation. The black arrows indicate the π–π stacking features within the *MPhene* nanosheets, revealing a stacking distance of 0.34 nm.

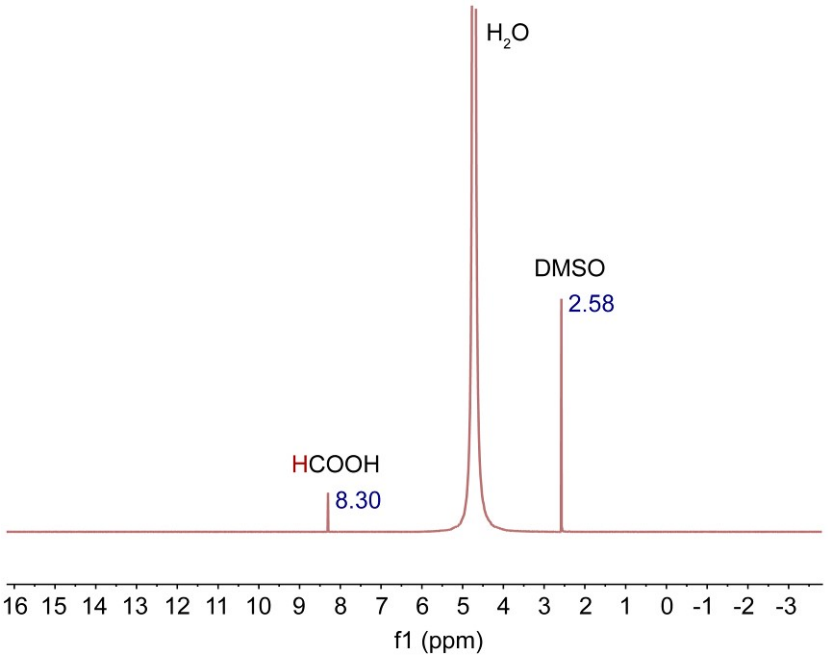

Fig. S12. ^{1}H NMR spectra of the liquid product during the process of electrochemical CO_2 reduction. The NMR spectra clearly showed that formic acid could be produced at –0.9 V.

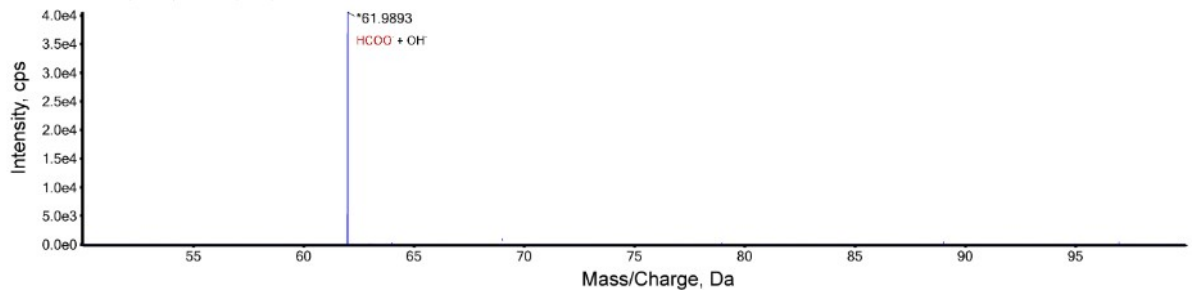

Fig. S13. Mass spectra of the liquid product during the process of electrochemical CO_2 reduction. The mass spectra clearly showed that formic acid could be produced at –0.9 V.

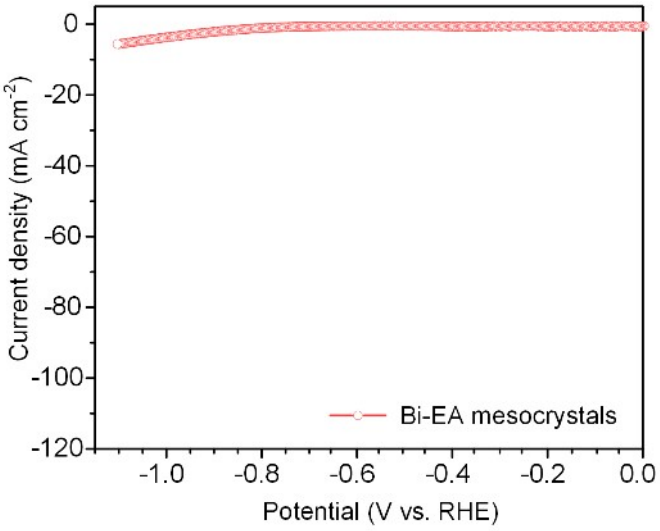

Fig. S14. LSV curve of Bi-EA mesocrystals in CO_2-saturated 0.5 M $KHCO_3$. The LSV curve manifested a significantly smaller current density compared with the *MPhene*.

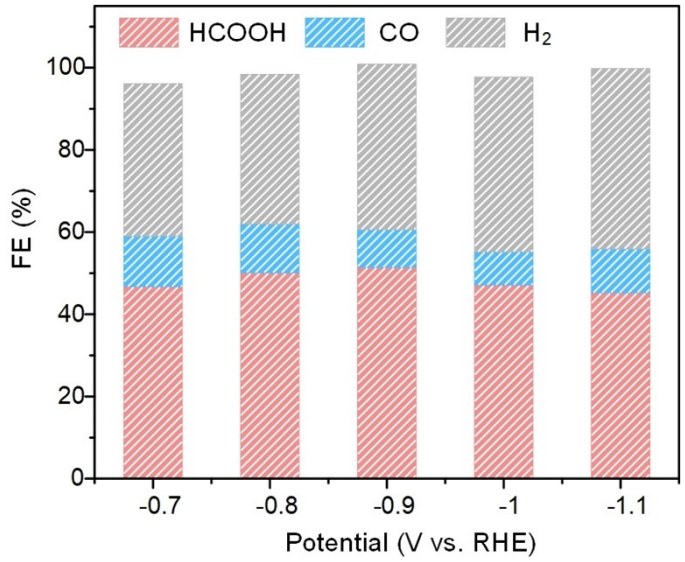

Fig. S15. Faradaic efficiencies (FE) of products for Bi-EA mesocrystals in CO_2-saturated 0.5 M $KHCO_3$. The FE of HCOOH (< 52%) is significantly lower than the *MPhene* (> 90%) in a wide potential window (from –0.7 to –1.1 V).

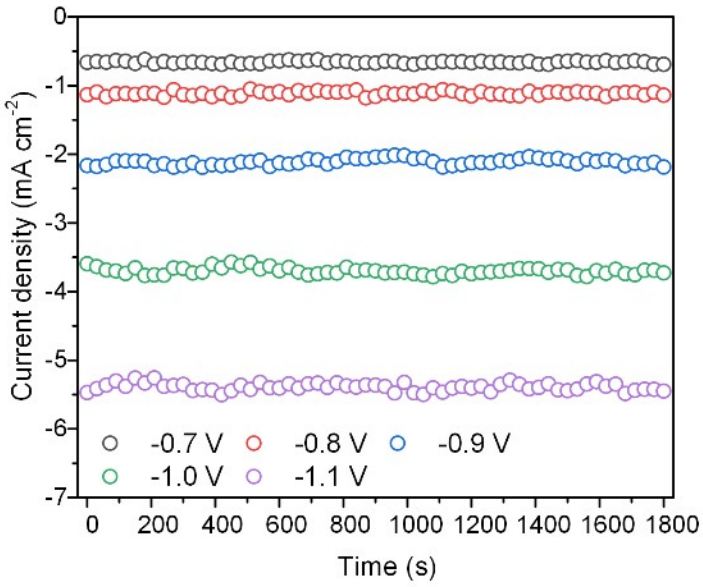

Fig. S16. Chronoamperometric curves of Bi-EA mesocrystals at different potentials. The current density of Bi-EA mesocrystals is significantly lower than *MPhene* in a wide potential window (from –0.7 to –1.1 V).

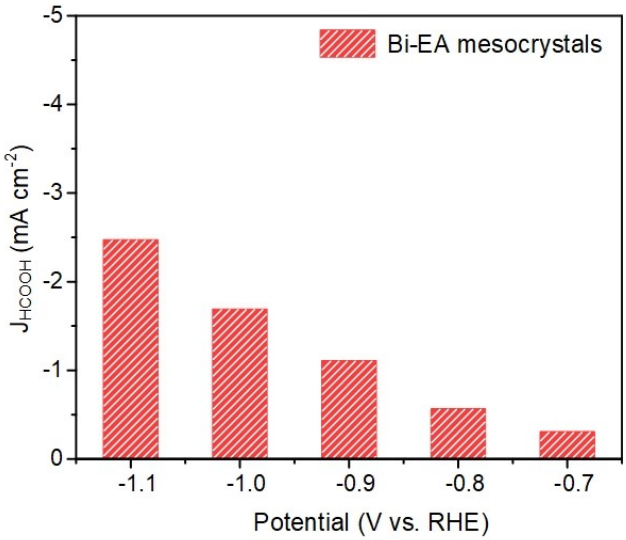

Fig. S17. HCOOH partial current density (J_{HCOOH}) of Bi-EA mesocrystals. The J_{HCOOH} of Bi-EA mesocrystals (< 3 mA cm^{-2}) is much lower than *MPhene* (> 90 mA cm^{-2}) in a wide potential window (from –0.7 to –1.1 V).

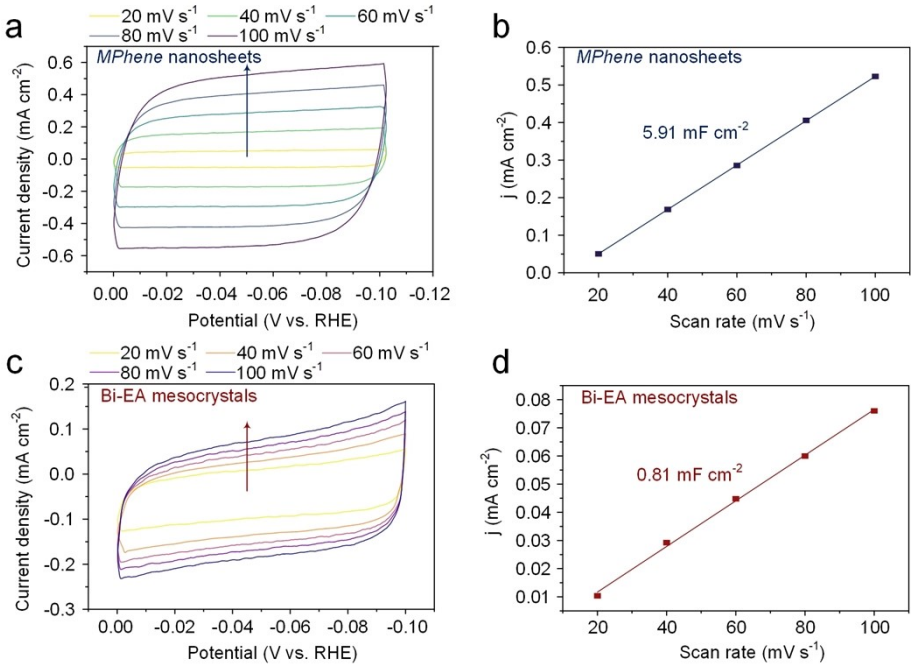

Fig. S18. (a) CV curves of *MPhene* nanosheets at different scan rates. (b) Capacitance values of *MPhene* nanosheets. (c) CV curves of Bi-EA mesocrystals at different scan rates. (d) Capacitance values of Bi-EA mesocrystals.

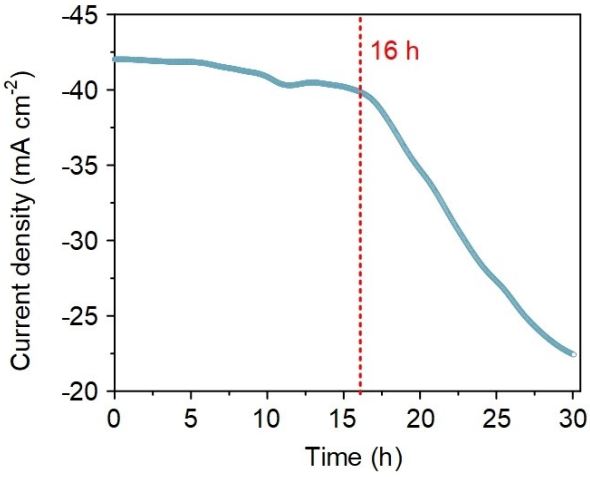

Fig. S19. Electrocatalytic stability assessment of *MPhene* nanosheets at −0.9 V *vs* RHE during 30-hour CO_2 electroreduction.

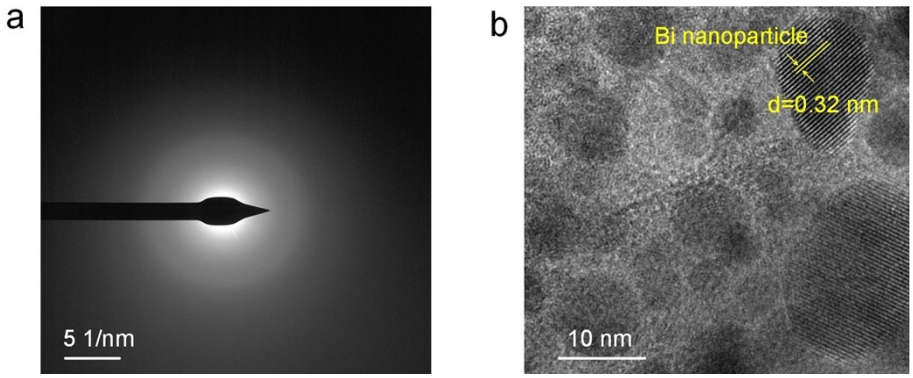

Fig. S20. Post-16-hour CO_2 electroreduction analysis of *MPhene* nanosheets. (a) SAED pattern of organic domains exhibiting diffuse ring patterns, indicative of disrupted supramolecular periodicity. (b) HRTEM image revealing Bi metal lattice fringes (d-spacing = 0.32 nm, consistent with Bi(110) planes) embedded within the nanosheet matrix.

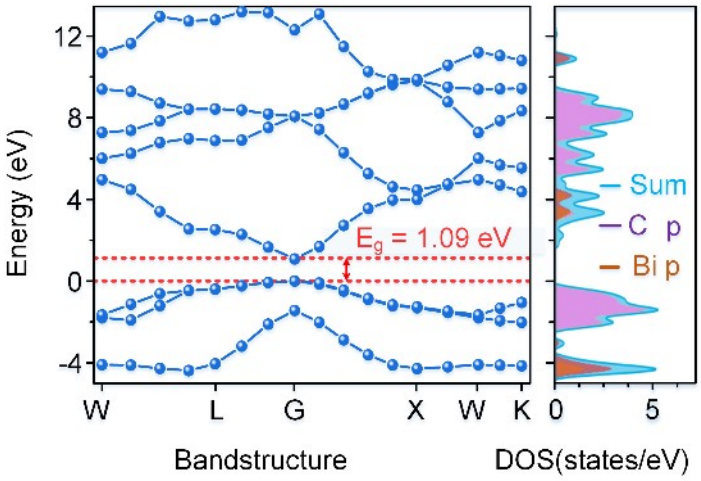

Fig. S21. Calculated bandstructure (left) and corresponding density of states (right) of *OCHO intermediate. The narrower bandwidth of the *OCHO intermediate (1.09 eV) illustrated an improved conductivity, which was responsible for the effective transformation of the *OCHO intermediate during the CO_2RR process.

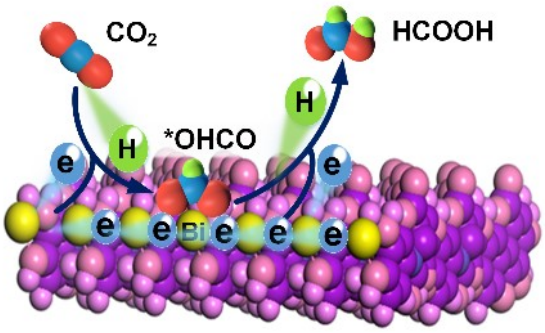

Fig. S22. Proposed mechanism of the CO_2RR process by *MPhene*.

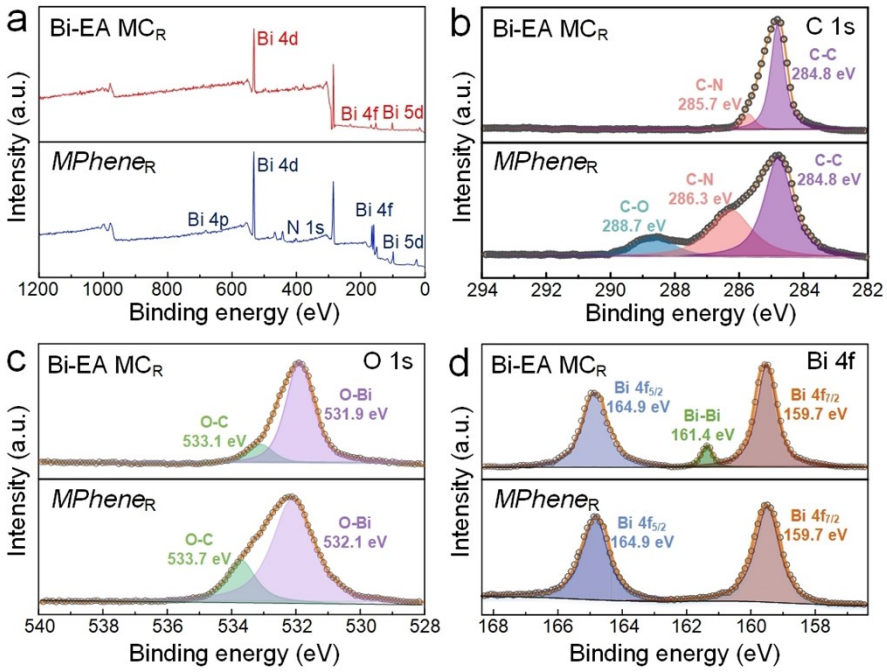

Fig. S23. XPS analyses of Bi-EA mesocrystals (Bi-EA MC_R) and *MPhene* (*MPhene*$_R$) after CO_2RR. (a) XPS survey spectra. High-resolution XPS spectra of (b) C 1s, (c) O 1s, and (d) Bi 4f. After CO_2RR, typical peaks of Bi-Bi can be observed in the Bi 4f XPS spectra of Bi-EA MC_R, indicating that partial Bi of Bi-EA mesocrystals was reduced during the CO_2RR process. Meanwhile, a sharp decrease in the spectra of Bi-EA MC_R suggests the destruction of the structure of Bi-EA mesocrystals during the CO_2RR process. However, the XPS spectra of *MPhene*$_R$ showed good integrity due to the fine electrical conductivity of *MPhene*.

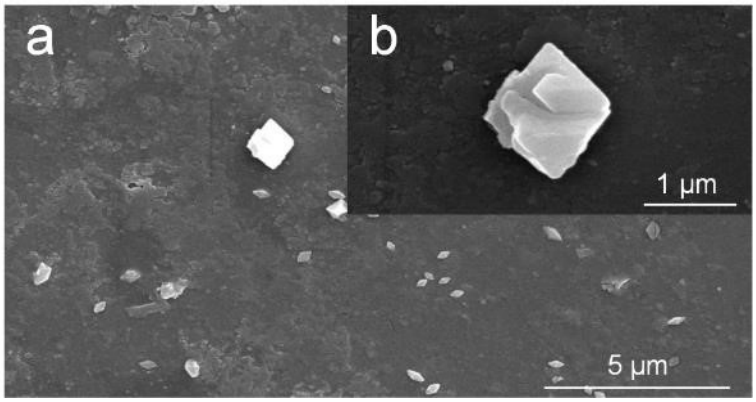

Fig. S24. SEM images of Bi-EA mesocrystals after CO_2RR. The result illustrated that the Bi-EA mesocrystals phase can be destroyed tremendously during the CO_2RR process due to poor electrical conductivity.

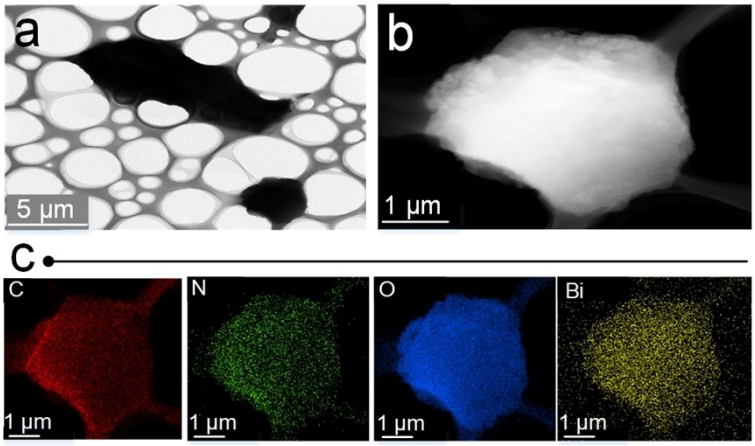

Fig. S25. (a) TEM, (b) HAADF-STEM, and (c) the corresponding EDS mapping images of Bi-EA mesocrystals after CO_2RR. The result illustrated that the Bi-EA mesocrystals phase can be destroyed tremendously during the CO_2RR process due to poor electrical conductivity.

Section S4. Supporting tables

Table S1. Statistical analysis of *MPhene* nanosheets based on AFM measurements over a large scan area.

NO.	Thickness (nm)	Length (μm)	Width (μm)	Lateral size[a] (μm)	Aspect ratio[b]
1	3.44	2.8903	0.7490	1.4713	427.71
2	3.4	2.4187	0.7556	1.3519	397.61
3	3.41	2.6164	0.8709	1.5095	442.67
4	3.48	2.3483	0.5799	1.1670	335.33
5	3.46	2.8798	0.7596	1.4790	427.46
6	3.39	3.6899	1.0401	1.9590	577.89
7	3.48	3.1888	1.0113	1.7958	516.03
8	3.11	3.0100	0.7598	1.5123	486.26
9	3.52	2.5609	0.6700	1.3099	372.13
10	3.43	3.8476	0.9643	1.9262	561.57
11	3.55	3.2477	0.7279	1.5375	433.11
12	3.45	4.1265	0.7411	1.7488	506.89
13	3.59	4.3225	0.8632	1.9316	538.06
14	3.43	6.2159	0.9516	2.4321	709.06
15	3.55	3.2802	0.9562	1.7710	498.88
16	3.40	3.4886	0.6631	1.5210	447.34
17	3.42	2.2277	0.7607	1.3018	380.64
18	3.5	3.3517	0.9263	1.7620	503.43
19	3.39	3.6075	0.7151	1.6062	473.79
20	3.64	3.6720	0.9881	1.9048	523.30
Averag e	3.45 ± 0.10	3.3496 ± 0.8716	0.8227 ± 0.1296	1.6499 ± 0.2895	477.96 ± 82.54

[a]The lateral size is calculated based on the following formula: $\text{Lateral size} = \sqrt{\text{Length} \times \text{Width}}$

[b]The aspect ratio is calculated based on the following formula: $\text{Aspect ratio} = \frac{\text{Lateral size}}{\text{Thickness}} \times 1000$

Table S2. Bi L3-edge EXAFS fitting parameters for *MPhene* nanosheets.

XAS edge	Sample	Shell	CN[a]	R[b] (Å)	σ^{2}[c] (Å^{2})	R factor[d]
Bi L3-edge	*MPhene*	Bi-O_1	1.9	2.16	0.005	0.011
		Bi-O_2	2.0	2.35	0.002	0.006

[a]CN: coordination number.

[b]R: interatomic distance.

[c]σ^{2}: Debye-Waller factor accounting for thermal and structural disorder.

[d]R factor: goodness of fit.

Table S3. Crystallographic data of *MPhene*.

Name	*MPhene*
Chemical composition	$Bi_4C_{96}H_{96}O_{40}N_8$
Mass formula	2837.74
Crystal system	triclinic
Space group	*P*1
a (Å)	13.8561(3)
b (Å)	9.5631(2)
c (Å)	8.5262(5)
α (°)	82.120(7)
β (°)	76.790(4)
γ (°)	77.780(7)
R_p	0.0325
R_{wp}	0.0412
R_{exp}	0.0391
Crystal density (g cm^{-3})	0.809

Table S4. CO_2RR comparison of sheet-based electrocatalysts in neutral electrolytes for formic acid production.

Samples	Potential (V *vs.* RHE)	Maximum FE_{HCOOH} (100%)	Maximum J_{HCOOH} (mA cm^{-2})	References
MPhene	**–0.7 ~ –1.1**	**93.2**	**115.5**	**This work**
Bi@graphene	–0.6 ~ –1.4	93.8	17.7	(3)
Bismuthene@BP	–0.5 ~ –1.0	98.0	54.0	(4)
CuO-NS	–0.9 ~ –1.4	27.3	17.1	(5)
Bi@MOF NS	–0.8 ~ –1.1	88.5	3.0	(6)
In-BDC NS	–0.4 ~ –1.1	88.0	6.5	(7)
PML-Cu NS	–0.6 ~ –1.0	80.9	18.1	(8)
CuTCPP NS	–0.6 ~ –0.8	68.4	5.1	(9)
a-SnBi NS/rGO	–0.3 ~ –0.6	4.4	0.3	(10)
$Bi_{0.6}Cu_{0.4}$ NS	–0.8 ~ –1.2	97.3	63.9	(11)
$Bi_{1,n}$-pBi_2O_{3-x} NS	–0.8 ~ –1.3	75.1	53.9	(12)
BiCuSeO NS	–0.4 ~ –1.1	93.4	47.5	(13)

Section S5. Supporting references

1 S. Gong, Y. Zhai, C. Jin, H. Xu, Q. Xia, W. Li, Y. Ying, J. Wu, X. She, Z. Wang, X. Lv, C. Wu, K. Chan, X. Zhao, X. Zhang, S. P. Lau, Interface engineering of single-molecular heterojunction catalysts for CO_2 electroreduction in strong acid medium. *Nat. Commun.* **2025**, *16*, 8704.

2 X. Qiu, X. Wang, Y. He, J. Liang, K. Liang, B. L. Tardy, J. J. Richardson, M. Hu, H. Wu, Y. Zhang, O. J. Rojas, I. Manners, J. Guo, Superstructured mesocrystals through multiple inherent molecular interactions for highly reversible sodium ion batteries. *Sci. Adv.* **2021**, *7*, eabh3482.

3 S. Liu, X. F. Lu, J. Xiao, X. Wang, X. W. Lou, Bi_2O_3 nanosheets grown on multi-channel carbon matrix to catalyze efficient CO_2 electroreduction to HCOOH. *Angew. Chem. Int. Ed.* **2019**, *58*, 13828–13833.

4 F. Yang, A. O. Elnabawy, R. Schimmenti, P. Song, J. Wang, Z. Peng, S. Yao, R. Deng, S. Song, Y. Lin, M. Mavrikakis, W. Xu, Bismuthene for highly efficient carbon dioxide electroreduction reaction. *Nat. Commun.* **2020**, *11*, 1088.

5 P. Wang, S. Meng, B. Zhang, M. He, P. Li, C. Yang, G. Li, Z. Li, Sub-1 nm Cu_2O nanosheets for the electrochemical CO_2 reduction and valence state–activity relationship. *J. Am. Chem. Soc.* **2023**, *145*, 26133–26143.

6 X. He, Y. Guo, J. Zhang, S. Yang, J. Chen, S. Li, S. Xie, Y. Wang, C. Wang, Why can poorly conductive Bi@UiO-MOF catalyze CO_2 electroreduction? *Chem. Commun.* **2023**, *59*, 5737–5740.

7 S.-Z. Hou, X.-D. Zhang, W.-W. Yuan, Y.-X. Li, Z.-Y. Gu, Indium-based metal–organic framework for high-performance electroreduction of CO_2 to formate. *Inorg. Chem.* **2020**, *59*, 11298–11304.

8 D. Yang, S. Zuo, H. Yang, Y. Zhou, X. Wang, Freestanding millimeter-scale porphyrin-based monoatomic layers with 0.28 nm thickness for CO_2 electrocatalysis. *Angew. Chem. Int. Ed.* **2020**, *59*, 18954–18959.

9 J.-X. Wu, S.-Z. Hou, X.-D. Zhang, M. Xu, H.-F. Yang, P.-S. Cao, Z.-Y. Gu, Cathodized copper porphyrin metal–organic framework nanosheets for selective formate and acetate production from CO_2 electroreduction. *Chem. Sci.* **2019**, *10*, 2199–2205.

10 X. Chen, S. Lv, H. Gu, H. Cui, G. Liu, Y. Liu, Z. Li, Z. Xu, J. Kang, G. Teobaldi, L.-M. Liu, L. Guo, Amorphous bismuth–tin oxide nanosheets with optimized C–N coupling for efficient urea synthesis. *J. Am. Chem. Soc.* **2024**, *146*, 13527–13535.

11 H. Liu, Y. Bai, M. Wu, Y. Yang, Y. Wang, L. Li, J. Hao, W. Yan, W. Shi, A regenerable Bi-based catalyst for efficient and stable electrochemical CO_2 reduction to formate at industrial current densities. *Angew. Chem. Int. Ed.* **2024**, *63*, e202411575.

12 M. Zhang, W. Zhu, Z. Liu, S. Chen, D. Zhou, X. Mu, Z. Zhuang, S. Wang, J. Yang, Y. Du, X. Luo, Q. Zhang, S. Liu, D. Wang, Z. Dai, Selective sieving effect of multi-atomic bismuth interfaces for efficient formate electrosynthesis and evolution at industrial current density. *Angew. Chem. Int. Ed.* **2025**, e202510206.

13 J. Duan, T. Liu, Y. Zhao, R. Yang, Y. Zhao, W. Wang, Y. Liu, H. Li, Y. Li, T. Zhai, Active and conductive layer stacked superlattices for highly selective CO_2 electroreduction. *Nat. Commun.* **2022**, *13*, 2039.